Analyst

PAPER

View Article Online
View Journal

Cite this: DOI: 10.1039/c9an01230c

Microparticle separation using asymmetrical induced-charge electro-osmotic vortices on an arc-edge-based floating electrode†

Xiaoming Chen,[a] Yukun Ren, *[a,b,c] Likai Hou,[a] Xiangsong Feng,[a] Tianyi Jiang[a] and Hongyuan Jiang*[a,b]

Five arc-shaped gaps were designed on the bipolar electrode to actuate alternately opposite-direction asymmetrical induced-charge electro-osmosis (AICEO) vortices, and we developed a microfluidic device using such asymmetrical vortices to realize particle separation. When the buoyancy force dominates in the vertical direction, particles stay at the channel bottom, experiencing a left deflection under the vortices in the convex arc areas. In contrast, when the levitation force induced by AICEO vortices overcomes the buoyancy force, particles are elevated to a high level and captured by right vortices, undergoing a right deflection under the vortices in the concave arc areas. Moreover, when particles pass through the concave or convex arc areas every time, their right or left deflections are enlarged gradually and the separation becomes more complete. Remarkably, as the light/small particles at low voltage, heavy/large particles can be elevated to a new high level and undergo right deflection by increasing the voltage. We first explicitly proved the separation principle and analyzed numerically its capability in density- and size-based separation. Depending on the study of the voltage-dependent AICEO characterization of 4 μm silica and 4 μm PMMA particles, we experimentally verified the feasibility of our device in density-based separation. According to the investigation of sensitivity to particle size, we separated multi-sized yeast cells to confirm the capability of our device in size-based separation. Finally, we extracted yeast cells from impeding particles, obtaining 96% purity. Additionally, we designed a 500 μm distance between the focusing and separation region to circumvent the problems caused by electric-field interaction. Our AICEO-based separation method holds potential to serve as a useful tool in transesterification of microalgal lipids to biodiesel and solar cell processing because of its outstanding advantages, such as gentle conditions, contact-free separation, high-sensitivity and high-efficiency separation capability.

Received 2nd July 2019,
Accepted 15th July 2019

DOI: 10.1039/c9an01230c

rsc.li/analyst

Introduction

Separation is central in a broad range of applications such as preprocessing of chemical reaction samples,[1–3] early diagnosis of cancers,[4–8] environmental monitoring,[9–12] intercellular communication investigations,[13,14] transesterification of microalgal lipids to biodiesel,[15,16] and solar cell processing.[17,18] Among the various available separation techniques involving analytical ultracentrifugation,[9,19] viscoelastic effects,[4,10,20,21] acoustofluidic platforms,[5,13] magnetic manipulation[15,22,23] and dielectrophoresis (DEP),[24–30] vortices provide a gentle and promising method of separation in isolating particles with differences in physical properties.[31,32]

Vortex-based separation of particles was illustrated some years ago.[31,33] In 2002, Benczik and coworkers studied the selective sensitivity of open chaotic flows on the inertia and size of the particles and asserted that this principle can be implemented into the design of particle-mixture separators.[31] In 2007, Vilela and coworkers demonstrated the permanent trapping of an aerosol of density higher than that of the vortex fluid. Trapping occurred in various cases, regardless of the nonhyperbolicity of the passive advection and whether gravitational effects are present.[32] Moreover, they also mentioned that the trapping of heavy particles in the vortex system may be useful in industrial applications for the separation of mixed particles of different sizes. In 2014, Angilella and coworkers studied inertial particle trapping in a vertical open flow com-

[a]School of Mechatronics Engineering, Harbin Institute of Technology, Harbin 150001, PR China. E-mail: rykhit@hit.edu.cn
[b]State Key Laboratory of Robotics and System, Harbin Institute of Technology, Harbin 150001, PR China. E-mail: jhy_hit@hit.edu.cn
[c]State Key Laboratory of Nonlinear Mechanics, Chinese Academy of Sciences, Beijing 100190, PR China

†Electronic supplementary information (ESI) available. See DOI: 10.1039/c9an01230c

posed of a pair of vortices,[34] which in theory exhibited significant guidance from vortices to have value in particle separation. To date, although many kinds of vortices are known, controlling their position and vorticity precisely for flexible manipulation of particles in a fluid still remained elusive. More importantly, continuous vortex-based particle separation needs steady and long-lived vortices. These aspects limit the development of vortex-based separators in continuous flow.

In the past two decades, considerable attention has been drawn towards the induced-charge electro-osmosis (ICEO) flow.[35–39] Because the gravitational force is important, particles cannot be trapped by the ICEO vortices; they escape to the flow stagnation line (FSL), contributing to a particle stream.[40–42] Based on this, many devices were developed to concentrate and direct micro-samples.[43,44] Our group also took advantage of the ICEO focusing characterization of particles to improve the current DEP-based separation chip, thereby bypassing the cumbersome peripheral system and the complicated operation needed to achieve hydrodynamic squeezing.[45] Moreover, stable ICEO vortices can exist on the bipolar electrode and their vorticity, including pattern and strength, can be controlled flexibly and accurately by adjusting the frequency and intensity of the input AC signal.[46–48] Recently, particle beam switching *via* asymmetrical ICEO (AICEO) vortices was reported, which shows good potential of AICEO vortices in particle separation for its controllable lateral driving force.[49] Although that device presents good performance in particle beam switching, the profiles of vortices in the deflection region make it show serious limitations and weaknesses in particle separation. Moreover, when separating particles, interaction between upstream and downstream electric fields causes undesired deflection and serious particle leakage, making the operation more complicated and the result more unexpected. Hence, to date, an effective and reliable device for particle separation using AICEO vortices may not have been developed. Importantly, prominent advantages of AICEO vortices, involving gentle operation environment and contact-free operation process, and controllable driving force in vertical and horizontal directions, make it hold good potential in the isolation of uniform-sized graphene oxide sheets for the fabrication of biosensors[50,51] and separation of microalgae for biodiesel.[15] The current situation enthused us to develop an effective AICEO-vortex-based separation device.

The shapes of the floating electrode edge have a certain effect on the ICEO vortex profile in a fixed electric field, because the slip velocity on the polarizable surface varies with the square of the applied voltage.[38] This inspired us to design some arc gaps on the floating electrode to break the symmetrical ICEO vortices more obviously, which is shown in Fig. 1b, schematically. On the one hand, the ICEO vortices in the convex arc regions are stronger in power than their opposing vortices from the sudden change in the electric field in this region. On the other hand, the vortices in the concave arc areas are so weak that they are overcome by their opposites

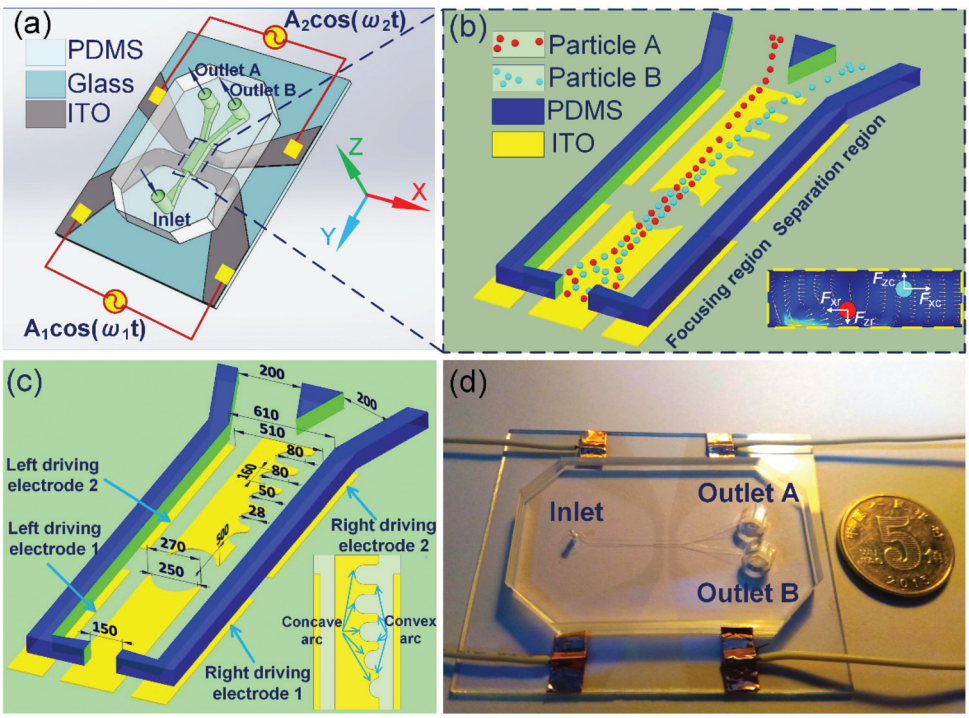

Fig. 1 Schematic images and photograph of the device. (a, b) Illustration of the chip configuration and separation principle. In the insert to (b), F_{xr}/F_{xc} is the drag force from combined flow field experienced by red/cyan particles in the *X* coordinate, F_{zr}/F_{zc} is the resultant force of buoyancy and upward drag, experienced by red/cyan particles in the *Z* coordinate. (c) The specific dimension (in units of microns) of the structure. (d) Photograph of the actual device.

because of the weak electric field at this edge. Under this scenario, opposite-direction asymmetrical vortices are alternately actuated both in the convex and concave arc areas of the floating electrode, producing left and right push forces. It is worth noting that the FSL on the channel bottom is no longer a straight line but is deflected toward the left-hand side. When the particles pass through this floating electrode, the AICEO vortices force particles to escape from the vortices and move towards the FSL under a relatively low voltage intensity at low frequency. Thus, under the sustained action of the AICEO vortices in the convex arc areas, the particle stream experiences a deflection towards the left-hand side. If the voltage intensity is increased, then the vortex strength is sufficient to promote the particles to a higher level. Under this circumstance, the particles are pushed away from their original trajectory, along the FSL, by the vortices in the concave arc areas, resulting in a reverse deflection. Moreover, the left or right (positive or negative) deflection of the particle stream will be enlarged, when they pass through the convex or concave arc areas, leading to high-efficiency separation (definition of deflection is given in Fig. S1†). Remarkably, the states of the particles, staying at the channel bottom or being elevated to a new equilibrium height, can be switched by accurately tuning the voltage input, promoting the sensitivity of this method in density- and size-based separation.

Based on the study of arc-edge-based floating electrodes, we proposed a novel method of particle separation. The device includes two modules integrated in series, a classic bipolar electrode to generate symmetrical ICEO vortices to focus particles into a fine particle stream and an arc-edge-based floating electrode to form AICEO vortices to separate the particles. A 500 μm distance between the two floating electrodes with a 250 μm arc was designed to suppress the interaction of the upstream and downstream electric fields, which ensures that particle samples enter the separation region from the same position and experience the same vortex field to obtain stable separation. Firstly, we built a physical model to study the vortex distribution at different channel cross sections and the velocity distribution on the different channel levels. Secondly, we explicitly proved the separation criteria and analysed numerically the detail mechanisms in density- and size-based separation. Thirdly, we investigated the focusing and deflection characterization of 4 μm polymethyl methacrylate (PMMA) and 4 μm silica microbeads, and we separated these two kinds of particles to confirm experimentally the feasibility of our device in density-based separation. Fourthly, depending on numerical simulations to study the sensitivity to particle size, we separated multi-sized yeast cells to validate the capability of this method in size-based separation. Finally, we took advantage of our method to separate uniform-sized yeast cells and silica particles, and investigated the conductivity-dependent separation processes. Advantages of this effective separation method, such as gentle operation conditions, contact-free separation process, and high-efficiency and high-sensitivity separation capability, make it a superior candidate in areas of applications such as water-quantity monitoring, solar cell processing, and transesterification of microalgal lipids to biodiesel.

Materials and methods

Device design and fabrication

Mixed particles were focused into a fine particle stream by the symmetrical ICEO vortices in the focusing region, the entrance of which is a horn-shaped structure to enhance focusing. Five arc-shaped gaps (with different distances to the channel centerline) of the bipolar electrode were designed to alternately generate opposite-direction AICEO vortices in the separation model by analyzing the effect of the gap shape on the AICEO transverse velocity theoretically (see Fig. S2 in the ESI†). The separated particles are directed into the desired branches each having the same width of 200 μm and located at the end of the main channel. Fig. 1a shows the overall structure of the device. Details of the electrode configuration and the separation principle of the chip are illustrated in Fig. 1b. The buffer solution containing the mixed particles (particles A and B) was injected into the PDMS-based channel from the inlet. Under the action of the symmetrical ICEO vortices, a mixture of particles is focused into a slender particle stream in the focusing region. In the separation region, the AICEO vortices deflect the particles from their original trajectory, along the symmetry axis of the channel.

Micro-beads experience the action of Stokes drag force along the X coordinate, $\boldsymbol{F}_x = 6\pi a\mu(\boldsymbol{u}_\mathrm{p} - \boldsymbol{u}_\mathrm{f})$. When $\boldsymbol{F}_x > 0$, particles experience right drag force, whereas when $\boldsymbol{F}_x < 0$, particles undergo left drag force. Along the Z coordinate, microbeads are subjected to the joint action of Stokes drag force and buoyancy force, $\boldsymbol{F}_z = 6\pi a\mu(\boldsymbol{w}_\mathrm{p} - \boldsymbol{w}_\mathrm{f}) + (m_\mathrm{p} - m_\mathrm{f})\boldsymbol{g}$. Red particles suspended near the bottom under the effect of $\boldsymbol{F}_{zr} < 0$ are pulled toward the left-hand side by $\boldsymbol{F}_{xr} < 0$, whereas cyan particles are elevated to a higher level by $\boldsymbol{F}_{zc} > 0$ and pushed toward the right-hand side by $\boldsymbol{F}_{xc} > 0$. Fig. 1c gives the specific dimensions in units of microns. The photograph of the actual microfluidic chip is shown in Fig. 1d. In the experiment, the left and right driving electrode 1 were at an electric potential of $\Phi_1 = A_1\cos(\omega_1 t)$ and $\Phi_1 = 0$. In the separation region, the left driving electrode 2 was applied with an AC signal $\Phi_2 = A_2\cos(\omega_2 t)$, whereas the right driving electrode 2 was grounded. Details of the processing of chip fabrication can be found in our previous reports.[40,45,52] The device fabrication consists of three steps briefly as shown in Fig. S3:† ITO-based electrode patterning, polydimethylsiloxane (PDMS)-based channel fabrication, and alignment and bonding. First, a thin film of transparent indium-tin-oxide (ITO) material coated on the glass slide was processed into the desired electrode structure using standard soft lithography and etching. Second, in fabricating a PDMS-based channel, we used a mold of dry-film resist (Riston SD238, DuPont, USA), which was processed in advance by soft lithography. Finally, after a surface treatment with oxygen plasma, the ITO-based electrode and the PDMS-based channel were aligned and integrated under a microscope (BX53, Olympus, Tokyo, Japan).

Sample preparation and system setup

4 μm silica (ρ = 2.20 g cm^{-3}) and 4 μm PMMA (ρ = 1.18 g cm^{-3}) microbeads (Sigma, USA) were suspended in KCl solution. Dry

yeast cells were revived in 20 °C DI water for 20 minutes and cultured in 50 °C DI water for two hours to obtain uniform-sized yeast cells (Fig. S4a†). Revived dry yeast cells were cultivated for two days to obtain multi-sized yeast cells (Fig. S4b†).[53–55] To obtain pure uniform- and multi-sized yeast cells, cultured yeast cells were centrifuged for 40 s in a centrifuge at r = 3000 rpm and washed in an ultrasonic machine for 40 s. This procedure was repeated six times.

Microparticle performances were observed and imaged using a microscope with a high CCD camera (Retiga-2000R, Qimaging, Surrey, BC, Canada). The input AC signal was generated from a functional generator (TGA12104). The numerical simulation was conducted in a FEM software, Comsol Multiphysics 5.3. To establish an AICEO characterization of the particles, we defined two indexes, focusing width W and deflection D, as shown in Fig. S1.†

Principles of ICEO separation

Particle focusing in symmetrical ICEO vortex pairs

Under the action of a normal electric field stimulated by the low-frequency AC signal on the driving electrode, counter ions in the saline solution are transported to the interface of the floating electrode and the electrolyte. After a characteristic RC charge relaxation time, a steady induced double layer (IDL) appears on the polarizable interface.[56] Moreover, the induced charges in the IDL screen the normal electric field, turning the floating electrode into an ideal insulator.[38] Under this circumstance, the tangential electric field exerts a force on the bipolar ionic charge within the IDL, providing a nonlinear electro-osmotic flow.[36] Moreover, the ICEO flow near the interface engenders vortices from the bulk fluid flow.[42] With the symmetrical arrangement of the electrode and the channel configuration, a pair of symmetrical ICEO vortices is formed on the floating electrode. Because the effect of gravity is non-ignorable, the particles cannot move toward the vortex core in spiral traces in the vortex. On being subjected to a fluid flow near the bipolar electrode, the particles move toward the straight FSL (see ESI, section 1†). Under the sustained action of the vortex pairs, samples of massive particles are focused into a fine particle stream (Fig. 1b).[40]

Particle separation in the AICEO vortex pairs

On the arc-edge-based floating electrode, the transverse vortices in the convex arc areas overcome their opposing vortices; see Fig. 2a, b, d, f, h, and g. One reasonable explanation for these results is that the convex arc structure causes a sudden change in electric field, contributing to a larger tangential electric field. In contrast, the vortices in the concave arc areas are dominated by their opposing vortices (Fig. 2a, c, e, g, i and k). This phenomenon is attributable mainly to the weak electric field intensity at the concave arc edge.[36] Moreover, a quantitative illustration of the transverse flow rate along the five intersections of the cross sections 1, 3, 5, 7, 9/2, 4, 6, 8, 10 and the X–Y plane at distance 11 μm is exhibited in Fig. 2l/m and reveals that the arc-edge side wall disturbs the symmetrical flow of the ICEO vortices, enhancing/diminishing the transverse flow rate in the convex/concave arc areas. Consequently, the FSL on the channel bottom is no longer a straight line but reshaped by the AICEO vortices induced on the arc edges (Fig. 3a).

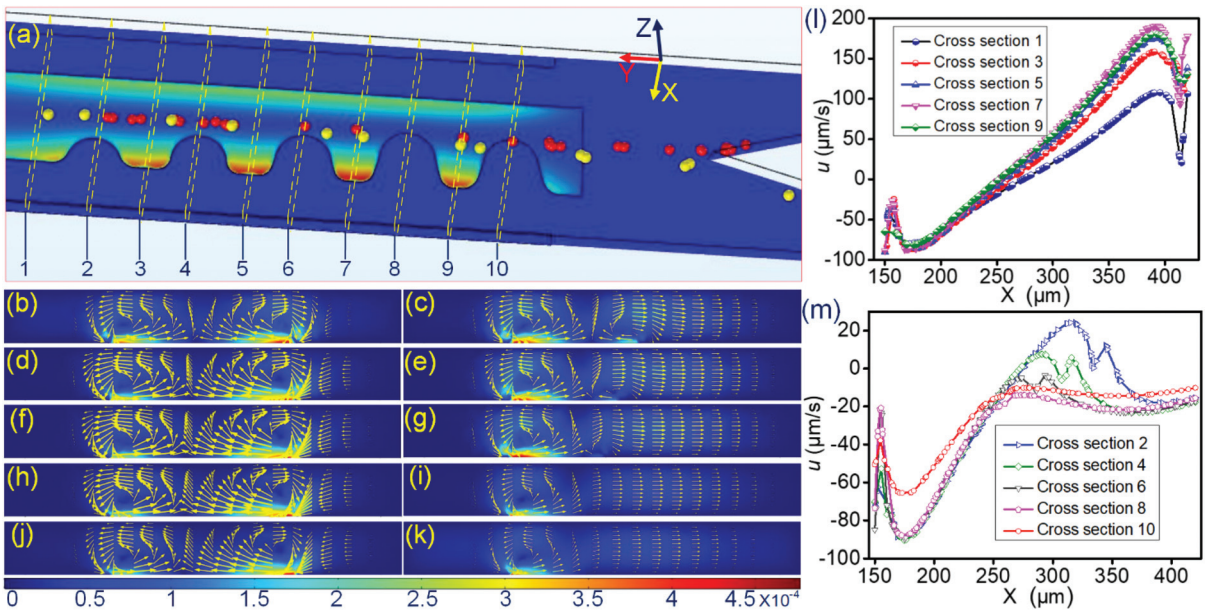

Fig. 2 Numerical simulations of the separation region at f_2 = 100 Hz and A_2 = 6 V. (a) Three-dimensional numerical simulation of the particle separation process. (b–k) The microstream in the X–Z cross sections 1–10 defined in (a). (l)/(m) The Y component of flow rate *versus* the intersections of the odd/even-numbered cross sections and the X–Y plane at a distance of 11 μm to the floating electrode.

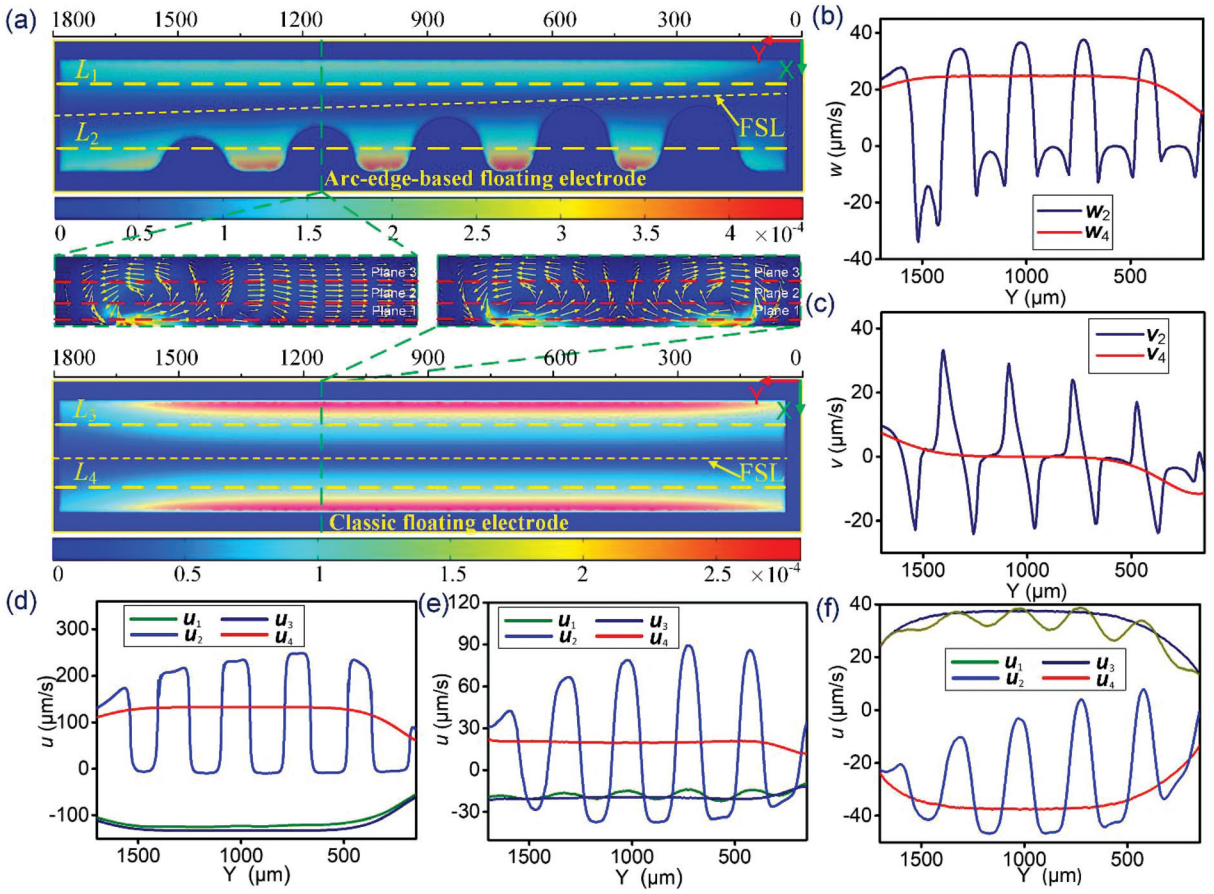

Fig. 3 The velocity distribution on the arc-edge-based and classic floating electrode at f_2 = 100 Hz and A_2 = 6 V. (a) Definition of cutting lines and planes. (Planes 1, 2, and 3 are X–Y planes at distances 4, 21, and 36 μm, respectively, from the floating electrode. L_1 and L_2/L_3 and L_4 are cut lines of distances 90 and −90 μm to the channel centerline on planes 1, 2, and 3 of the channel with an arc-edge-based/classic floating electrode.) (b) The Z component of flow rates, w_2 and w_4, along the cutting lines L_2 and L_4 on plane 2, respectively. (c) The Y component of flow rates, v_2 and v_4, along the cutting lines L_2 and L_4 on plane 2. (d–f) The transverse component of flow rate along the Y coordinate on different X–Y planes: (d) plane 1, (e) plane 2, (f) plane 3. u_1, u_2, u_3, and u_4 are the flow rates along the yellow cutting lines L_1, L_2, L_3, and L_4. To study the effect of arc edge on the transverse velocity, we introduced u_3 and u_4 for the channel with a classic bipolar electrode as they contrast with u_1 and u_2, for the channel with the floating electrode with arc-shaped gaps.

The velocity-field distributions on the arc-edge-based and classic floating electrode at f_2 = 100 Hz and A_2 = 6 V are shown in Fig. 3a. We also defined the cutting lines and planes on these two floating electrodes to study the effect of arc edges on the velocity field. The upward fluid flow can elevate particles to a higher level, and the forward fluid flow has accelerated or decreased the effect on particle motion along the Y coordinate. The upward/forward flow rates along L_2 and L_4 on plane 2 are shown in Fig. 3b/c. Compared with the almost-equal transverse flow rates u_3 and u_4 on both sides of plane 1, the amplitudes of u_1 and u_2 show an evident difference. u_1 exhibits an obvious fluctuation with large amplitude, whereas u_2 is slightly smaller than u_3. Moreover, u_1 and u_2 point toward the FSL (Fig. 3d). Therefore, if vortices have insufficient strength to carry the particles and move as vortices, the particles are diverted to the particle stream and confined along the FSL. Moreover, the resulting particle stream undergoes a deflection toward the left side under the sustained action of the AICEO vortices in the convex arc areas. As shown in Fig. 3e, the transverse flow rate, u_1, on plane 2 in the convex arc region still points to FSL, whereas in the concave region, u_1 becomes larger and begins to point to the right side. The amplitude of u_2 also exhibits a fluctuation and is nearly equal to u_4. Contrary to the transverse flow direction on plane 1, u_1 and u_3 on higher plane 3 point toward the left side and u_2 and u_4 point toward the right side (Fig. 3f). Remarkably, the transverse flow rate u_2 begins on average to overcome u_1, causing the particle stream to deflect toward the right side. If the AICEO vortices have adequate upward strength to overcome the buoyancy force, the particles will be promoted to a higher level and pulled toward the right side by the stronger opposing vortices. As a result, a compacted particle stream is deflected from the FSL toward the right side. Moreover, by increasing the voltage intensity continuously, the degree of deflection also continues to be enhanced. In this way, the particle stream experiences a wide range of deflections, switching from outlet A to B. In addition, under the

same upward hydrodynamic force derived from an AICEO flow, particles of different densities and sizes show unique focusing and deflection characteristics. Therefore, a fixed vortex profile induced by a specific AC signal produces a difference in trajectory for the two kinds of particles (details of the theoretical analysis are presented in ESI, sections 1–3†).

Depending on the above-mentioned flow-field analyses, the schematic diagrams demonstrating the separation principle device are shown in Fig. 4a and b. According to the side view, the upward drag force of yellow particles dominates the buoyancy force ($F_z > 0$), and yellow particles are elevated to a new level. From the top view, yellow particles experience a right deflection under lateral push force in the concave arc areas induced by vortices shown in Fig. 2c, e, g, i and k ($F_x > 0$). In contrast, the upward drag force of green particles can't overcome the buoyancy force ($F_z < 0$), and they stay at the channel bottom. Based on the top view, green particles undergo left deflection under the push force in the convex arc areas caused by the vortices shown in Fig. 2b, d, f, h and j ($F_x < 0$). Therefore, when $F_z > 0$, the particles are elevated to a higher level by the lateral push force $F_x > 0$ in every concave arc area, leading to a right deflection, whereas when $F_z < 0$, the particles stay at the channel bottom and experience a drag force $F_x < 0$ in every convex arc area, contributing to left deflection. Moreover, F_z can be adjusted by tuning the external electric field. Then, we numerically explored the capacity of the new device in density- and size-based separation based on the Lagrangian tracing method. We first studied the voltage-dependent deflection of 4 μm particles at the density of 2.20 and 1.18 g cm^{-3} (Fig. 4c). At the low voltage intensity, heavy and light particles both stayed at the channel bottom and experienced left deflection. By increasing the voltage intensity to 4 V, light particles began to be elevated to a higher level and experienced right deflection. Under this scenario, heavy particles still stayed at the channel bottom and underwent left deflection. By further increasing the voltage intensity to 7 V, the heavy particles also began to be levitated to a higher level and underwent right deflection at A_2 = 6 V and f_2 = 100 Hz.

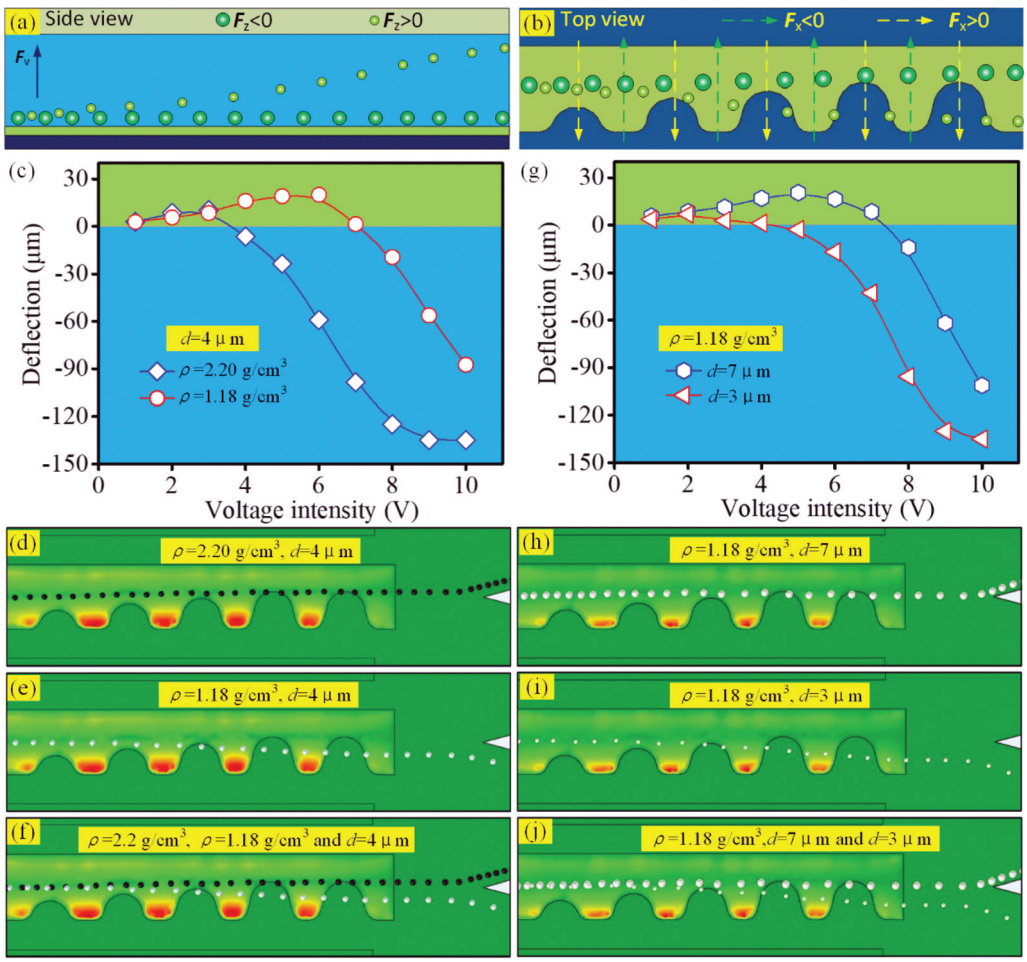

Fig. 4 Separation criteria. (a) and (b) Side and top view schematic diagrams illustrating the separation principle. (c) Dependence of deflection of particles with the density of 2.20 and 1.18 g cm^{-3}. (d/e) Trajectory of 4 μm particles with the density of 2.20/1.18 g cm^{-3} at A_2 = 6 V and f_2 = 100 Hz. (f) Separation behavior of the above-mentioned heavy and light particles. (g) Dependence of deflection of particles with the size of 7 μm and 3 μm. (h/i) Trajectory of particles (ρ = 1.18 g cm^{-3}) with the size of 7/3 μm at A_2 = 7 V and f_2 = 200 Hz. (j) Separation behavior of above-mentioned large and small particles.

Trajectories of heavy and light particles are given in Fig. 4d and e, and their separation process is given in Fig. 4f. We also investigated the voltage-dependent deflection of 7 μm and 3 μm particles with the same densities of 1.18 g cm^{-3} (Fig. 4g). In the voltage intensity range of 1–4 V, large and small particles remained at the channel bottom and experienced a left deflection. When the voltage intensity was over 4 V, small particles escaped from the channel bottom and experienced a right push force, leading to a right deflection. On increasing the voltage intensity to 8 V, large particles began to experience a right deflection. Trajectories of 7 μm and 3 μm particles are shown in Fig. 4h and i at A_2 = 7 V and f_2 = 200 Hz, and their separation process is shown in Fig. 4j.

Results and discussion

Density-based separation

Prior to density-based separation, we first experimentally studied the characterization of the 4 μm silica and 4 μm PMMA particles in the AICEO vortices in the separation region. With f_2 = 100 Hz and A_2 = 3 V, the PMMA particles were focused into a slender particle stream and maintained in the FSL of the AICEO vortex pairs, ending up in outlet A. When the voltage intensity was increased to 7 V, the PMMA particles were elevated to a higher level from the channel bottom and pushed toward the side wall of the arc edge with a deflection −108.34 μm, flowing into outlet B (Fig. 5a). Note that a faster flow rate in the Y component accelerated the motion of particles and led to a lower-number-density particle stream. A typical snapshot of the silica particles (Fig. 5b) shows that the particle stream experienced a deflection of 34.28 μm and was directed towards outlet A at f_2 = 100 Hz and A_2 = 3 V, whereas it had a deflection of −2.13 μm and flowed into outlet B at f_2 = 100 Hz and A_2 = 8 V. The particle within the AICEO flow possesses a common characteristic in which under a weak levitation force the particle stream experienced a positive deflection ending up in outlet A but under a strong lift force it underwent a negative deflection ending up in outlet B. The dependence of the focusing width and deflection of PMMA particles on voltage intensity (Fig. 5c and e) show that when the voltage intensity was increased from A_2 = 1 V to 3 V at f_2 = 100 Hz, the positive deflection of the PMMA particle stream slightly increased from 25.21 μm to 30.25 μm. Moreover, the focusing width obviously decreased from 25.21 μm to 13.28 μm. This change is attributable mainly to the fast flow rate in the Y direction under relatively strong voltage intensities, forming a low number density of particles and producing a slenderer particle stream. The X component of the ICEO flow near the arc edge overcame its opposite ICEO flow, which contributed to an increasing positive deflection. Note that for A_2 = 4 V, the vortices produced enough force to elevate the PMMA particles to a higher level (Fig. 5e). Under the effect of fluid flow in concave arc areas, the PMMA particles began to experience a right deflection. If the voltage intensity continued to increase to A_2 = 5 V, an evident right deflection emerged and the PMMA particles headed towards outlet B. When the voltage intensity was increased to 8 V, the deflection reached a limit value of −111.52 μm. In this process, the focusing width increased substantially from 13.28 μm to 53.42 μm in the interval of A_2 = 3 V to 7 V. Note that when the voltage intensity was over 8 V, a strong flow rate in the convex arc region pushes the particles towards the FSL but the fluid flow in the concave arc region pushed the particles towards the arc edge, thereby suppressing the regular pattern and motion of the particle stream (see ESI, Fig. S5†). A stronger vortex strength is required to elevate the silica particles; the dependence of the focusing width and deflection on voltage intensity are shown in Fig. 5d and f (photographs of the silica particles are given in ESI, Fig. S6†).

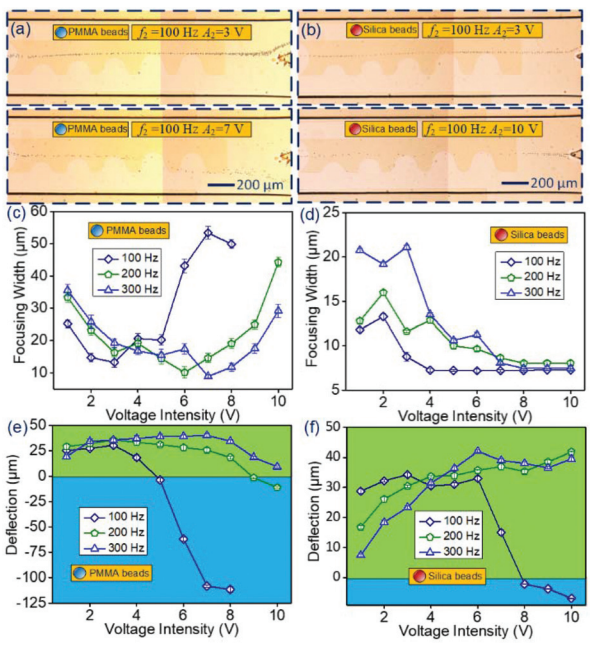

Fig. 5 AICEO characterization of PMMA and silica beads in the separation region. (a/b) Microphotographs of PMMA/silica micro-beads illustrating their focusing and deflection performance under different electric parameters. (c/d) Dependence of focusing width of PMMA/silica beads on voltage intensity under different frequencies. (e/f) Dependence of the deflection of PMMA/silica beads on voltage intensity at f_2 = 100, 200, and 300 Hz.

We conducted numerical simulations to study the features of this method in density-based separation. We changed the density of particles with the same diameter, 4 μm, to explore the sensitivity of this method in density-based separation.[57] When the densities of black and white particles are 2.5 g cm^{-3} and 1.0 g cm^{-3}, *i.e.*, the density difference is 1.5 g cm^{-3}, black particles are directed to outlet A, and white particles are diverted to outlet B (Fig. 6a). By decreasing the density difference to 0.5 and 0.25 g cm^{-3}, two kinds of particles all reached a designed position (Fig. 6b and c). When we further reduced the density difference to 0.125 g cm^{-3}, two kinds of particles were still directed to the desired outlets (Fig. 6d). We also numerically studied the voltage intensity dependence of combined force of 4 μm particles with different densities at f_2 = 100 Hz in the vertical direction (Fig. 6e). Light particles were elevated to a

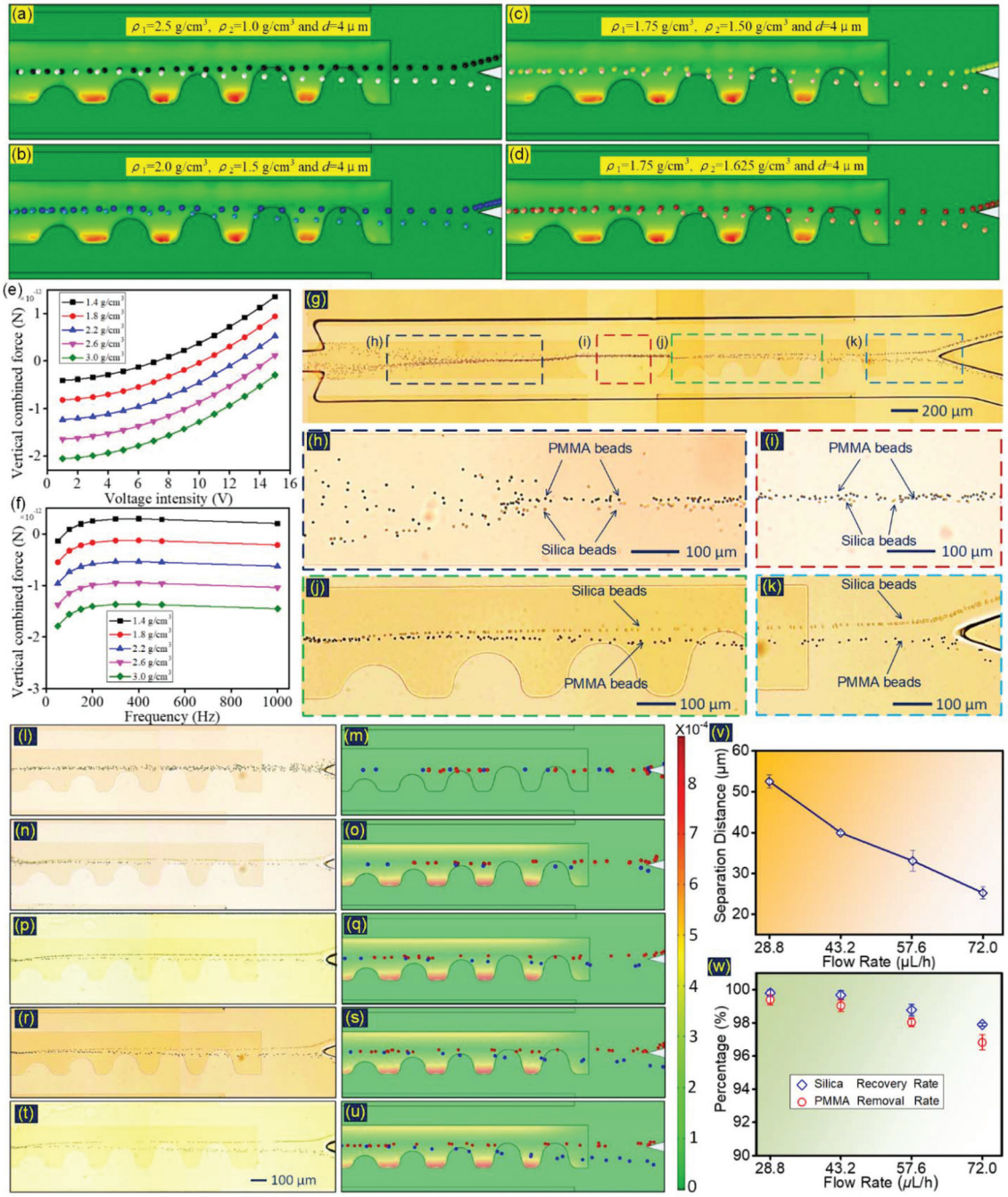

Fig. 6 Density-based separation. (a–d) Simulations studying the sensitivity of this method to particle density difference. (e–f) Voltage and frequency dependence of combined force of 4 μm particles with different densities. (g) Image showing the overall separation process of silica and PMMA particles at f_1 = 100 Hz, A_1 = 3 V, f_2 = 200 Hz, A_2 = 9 V and u = 43.2 μL h^{-1}. (h) All of the particles were focused into a fine particle stream by the symmetrical ICEO vortices in the focusing region. (i) Particle stream maintains a slender particle stream in the continuous flow. (j) Particle stream bifurcates under the AICEO vortices in the separation region. (k) Silica and PMMA particles are directed into outlets A and B, respectively. (g, h, i, j and k are superimposed images of several consecutive images produced using software Image J) (see ESI for a link to Movie S1.†) (l–u) Experimental and numerical results under different flow rates at f_1 = 100 Hz, A_1 = 3 V, f_2 = 100 Hz and A_2 = 7 V. (l) and (m) u = 72.0 μL h^{-1} with no AC signal, (n) and (o) u = 72.0 μL h^{-1}, (p) and (q) u = 57.6 μL h^{-1}, (r) and (s) u = 43.2 μL h^{-1}.(t) and (u) u = 28.8 μL h^{-1}. (v/w) Dependence of separation distance/efficiency and flow rate.

higher level and escaped from the channel bottom at low voltage intensity, whereas the levitation of heavy particles needed high voltage intensity. The frequency dependence of combined force of 4 μm particles at A_2 = 8 V is exhibited in Fig. 6f. According to Fig. 6f, the peak values of combined force in the vertical direction occurred at the frequency of 200 Hz.

We then investigated the performance of this method in density-based separation by isolating 4 μm silica and 4 μm PMMA microbeads. From Fig. 5e and f, the two particle types exhibited pronounced AICEO response discrepancies at f_2 = 200 Hz and A_2 = 10 V and they were directed into different outlets. Therefore, we chose this set of parameters to perform the separation experiment. A snapshot of the overall separation process in the microchannel is given in Fig. 6g (image was acquired with a 4× objective). A mixture of particles was focused into a fine particle stream with a focusing efficiency of nearly 100% under the symmetrical ICEO vortices in the focusing region at f_1 = 100 Hz and A_1 = 3 V (Fig. 6h). The particle stream maintained a rectilinear motion in the continuous flow (Fig. 6i). After entering the separation region, a clear and reliable separation was observed (Fig. 6j). The PMMA and silica particles experienced nearly the same upward hydrodynamic force from the fluid flow. Because this force can overcome the buoyancy force of the PMMA particles, they were promoted to a higher level and pushed away from their original trajectory. In contrast, the motion of silica was dominated by the downward buoyancy force. Silica particles cannot be elevated from the channel bottom by the hydrodynamic force and were transported to the FSL at the channel bottom. Consequently, the silica-particle stream subjected to a positive deflection ended up preferentially at outlet A, whereas the PMMA particle stream was more readily shifted towards the arc-edge side wall and ended up at outlet B (Fig. 6k) (images of Fig. 6h–k were obtained with a 10× objective).

We also studied the dependence of separation performance on the inlet flow rate. When no AC signal was applied across the separation region, the particle stream (a mixture of silica and PMMA) maintained a rectilinear motion and entered outlets A and B randomly at u = 72 μL h^{-1}, maintaining a fine stream (Fig. 6l and m). Once the input signal was applied, the silica particles are pushed towards the FSL and deflected to the left side, whereas PMMA particles were elevated from the channel bottom and dragged towards the arc-edge side wall at f_2 = 100 Hz, A_2 = 7 V and u = 72 μL h^{-1}. Under the repeated action of the AICEO vortices in the convex and concave arc areas, the positive and negative deflection of particles were further amplified, resulting in the silica-particle stream being directed toward outlet A and the PMMA-particle stream toward outlet B. The experimental results (Fig. 6n) were consistent with the numerical simulation (Fig. 6o). When the inlet flow rate was reduced to 57.6 μL h^{-1}, the separation distance was further amplified (Fig. 6p and q). With decreasing inlet velocity, the PMMA particle stream had a larger deflection and the silica particle trajectory showed no evident change, resulting in an increasing separation distance and an excellent separation performance. The separation processes of the experiments and simulations at u = 43.2 μL h^{-1} and u = 28.8 μL h^{-1} are shown in Fig. 6r, s and t, u, respectively. The voltage dependence of both the separation distance and separation efficiency is summarized in Fig. 6v and w. The separation efficiency always remains above 96% between u = 28.8 and 72.0 μL h^{-1}.

Size-based separation

After experimentally evidencing the feasibility of this method in density-based separation, we explored its capability in size-based separation. The combined force of levitation force and buoyancy force plays an important role in particle-stream deflection. We first studied the voltage intensity and frequency dependences of this combined force on the channel bottom. According to these curves demonstrating the force against voltage intensity, smaller particles were more readily poisoned at the high level and captured by right vortices in a fixed vortex profile (Fig. 7a). Moreover, with increasing voltage intensity, the upward flow rates were enhanced. Consequently, vortices have enough strength to elevate larger particles to a high level and make them move together with right vortices. It is worth noting that the combined forces in the vertical direction reached their peak value at the frequency of 200 Hz (Fig. 7b). Criteria of size-based separation are shown in Fig. 7c and d, schematically. When the concentrated particle stream passed through the concave arc area, in the same vortex profile, smaller particles were levitated to a new level and captured by right vortices. Under the horizontal drag force in concave arc areas, smaller particles underwent right deflection (Fig. 7c). When they passed through the convex arc areas, large particles experienced left deflection, because the right vortices dominate the left vortices in the convex arc areas (Fig. 7d). In this way, large and small particles produced their distinct trajectories due to their variation in size.

Then, we conducted numerical simulations to explore the sensitivity of this method in size-based separation. We first separated the 7 μm and 2 μm particles with the density of 1.75 g cm^{-3} at A_2 = 5 V and f_2 = 150 Hz (Fig. 7e). 7 μm particles experienced left deflection and ended up in outlet A, whereas 2 μm particles underwent right deflection and were directed into outlet B. We also reduced the size difference to 3 μm by separating the 6 μm and 3 μm particles at A_2 = 5 V and f_2 = 100 Hz (Fig. 7f). As a result, 6 μm and 3 μm particles were separated successfully and directed into the desired outlets. Size difference was further reduced to 1 μm by separating 5 μm and 4 μm particles (Fig. 7g) at A_2 = 5 V and f_2 = 100 Hz, and a good separation result was obtained. Therefore, the sensitivity of this method in size-based separation is less than 1 μm. When we separated the mixture of multi-sized particles, 1–7 μm, at A_2 = 6 V and f_2 = 150 Hz, we also obtained a good separation result (Fig. 7h and Movie S2†).

We further experimentally evidenced the capability of this method in size-based separation by manipulating yeast cells with various sizes (Movie S2†). The focusing process and rectilinear motion of multi-sized yeast cells are shown in Fig. 7i and j. Separation processes of multi-sized yeast cells under different parameters are shown in Fig. 7k–n. When the voltage intensity was 3 V at f_2 = 200 V, all the yeast cells were focused into particle stream at the FSL (Fig. 7k). By increasing the voltage intensity to 4 V at f_2 = 100 Hz, some small yeast cells overcame the buoyancy force and escaped from the particle

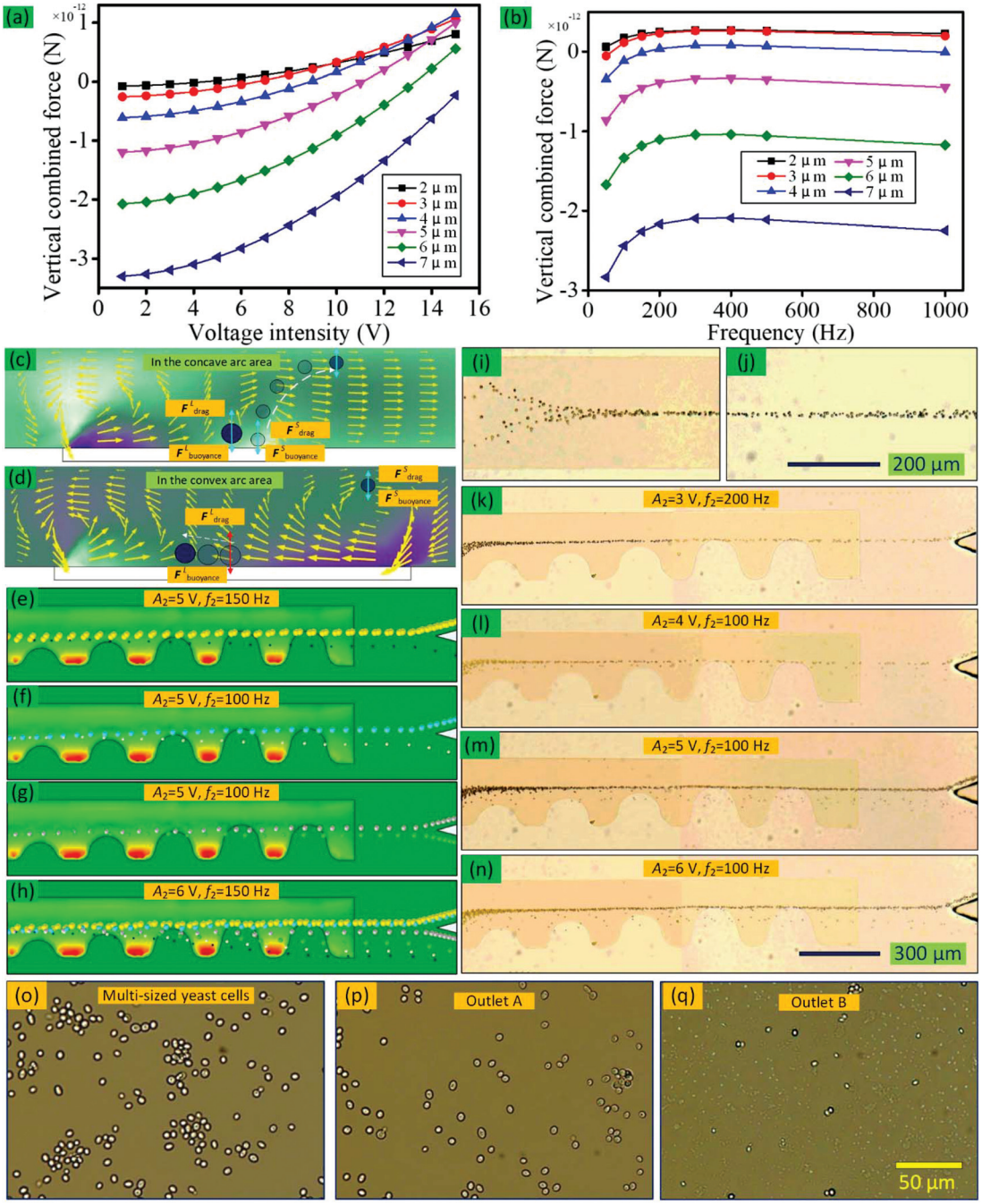

Fig. 7 Size-based particle separation. (a/b) Plots of vertical combined force against voltage intensity/frequency. (c and d) Schematic diagram illustrating the separation criteria. (e and h) Simulations exploring the sensitivity of this method to size difference. (e) Separation of 7 μm and 2 μm particles at A_2 = 5 V and f_2 = 150 Hz. (f) Separation of 6 μm and 3 μm particles at A_2 = 5 V and f_2 = 100 Hz. (g) Separation of 5 μm and 4 μm particles at A_2 = 5 V and f_2 = 100 Hz. (h) Separation of particles with the diameter of 1–7 μm at A_2 = 6 V and f_2 = 150 Hz. (i) Focusing process of various-size yeast cells. (j) Yeast cells maintaining rectilinear action in the connection region. (k–n) Separation performances of multi-sized yeast cells under different separation parameters. (o–q) Photographs of original multi-sized yeast cells and separated yeast cells obtained from outlets A and B at A_2 = 6 V and f_2 = 100 Hz.

stream, ending up in outlet B (Fig. 7l). When the voltage intensity was increased to 5 V at f_2 = 100 Hz, slightly large yeast cells were also separated from the particle stream (Fig. 7m). On increasing the voltage intensity to 6 V at 100 Hz, much larger yeast cells were extracted from the yeast-cell stream (Fig. 7n). The original multi-sized yeast cells are given in Fig. 7o, and separated yeast-cell samples obtained from outlet A and B at A_2 = 6 V and f_2 = 100 Hz are presented in Fig. 7p and q. Therefore, this method indeed presents good performance in size-based separation.

Separation of uniform-sized yeast cells and silica particles

Prior to separating silica particles and uniform-sized yeast cells, we investigated the behaviors of uniform-sized yeast cells in AICEO vortices. The yeast cells showed a remarkable analogous trend to the PMMA particles regarding the dependences of focusing width and deflection on voltage amplitude (Fig. 8a and b). Photographs illustrating the AICEO characterization of yeast cells are given in Fig. 8c and Fig. S7.† Furthermore, we took advantage of this method to purify yeast cells (Movie S3†). The separation process observed under a 4× objective at f_1 = 100 Hz, A_1 = 3 V, f_2 = 100 Hz and A_2 = 7 V is shown in Fig. 8d. Then, we studied the effect of the inlet flow rate on the obtained purity of cells for the above-mentioned parameter settings. Fig. 8e/f/g/h illustrate the separation behavior in the separation region under the flow rate of u = 86.4/72/57.6/28.8 μL h^{-1}, respectively. When the mixture of uniform-sized yeast cells and silica particles had entered the separation region, the original particle stream began to bifurcate. Yeast cells were directed into outlet B, whereas silica particles flowed into outlet A. According to the dependences of the separation distance and efficiency on the flow rate (Fig. 8i and j), the separation distance showed a decreasing trend with increasing flow rate. The purity always remains at a high level exceeding 96% in the interval u = 28.8 to 57.6 μL h^{-1}.

We also explored the conductivity-dependent performances of this method in the separation of silica particles and uniform-sized yeast cells (Fig. 9). At the conductivity of 100 μS cm^{-1}, the separation efficiency reached 96.1% and the separation distance reached 158.51 μm (Fig. 9a). By increasing the conductivity to 200 μS cm^{-1}, the separation efficiency and distance of this method reached 95.2% and 148.06 μm, respectively (Fig. 9b). On increasing the conductivity to 300 μS cm^{-1}, the separation distance was reduced to 97.54 μm and the separation efficiency was reduced to 93.2% (Fig. 9c). By further increasing the conductivity of the solution to 400 μS cm^{-1}, we still can obtain the good separation result with the separation distance of 70.12 μm and the separation efficiency of 92.4%

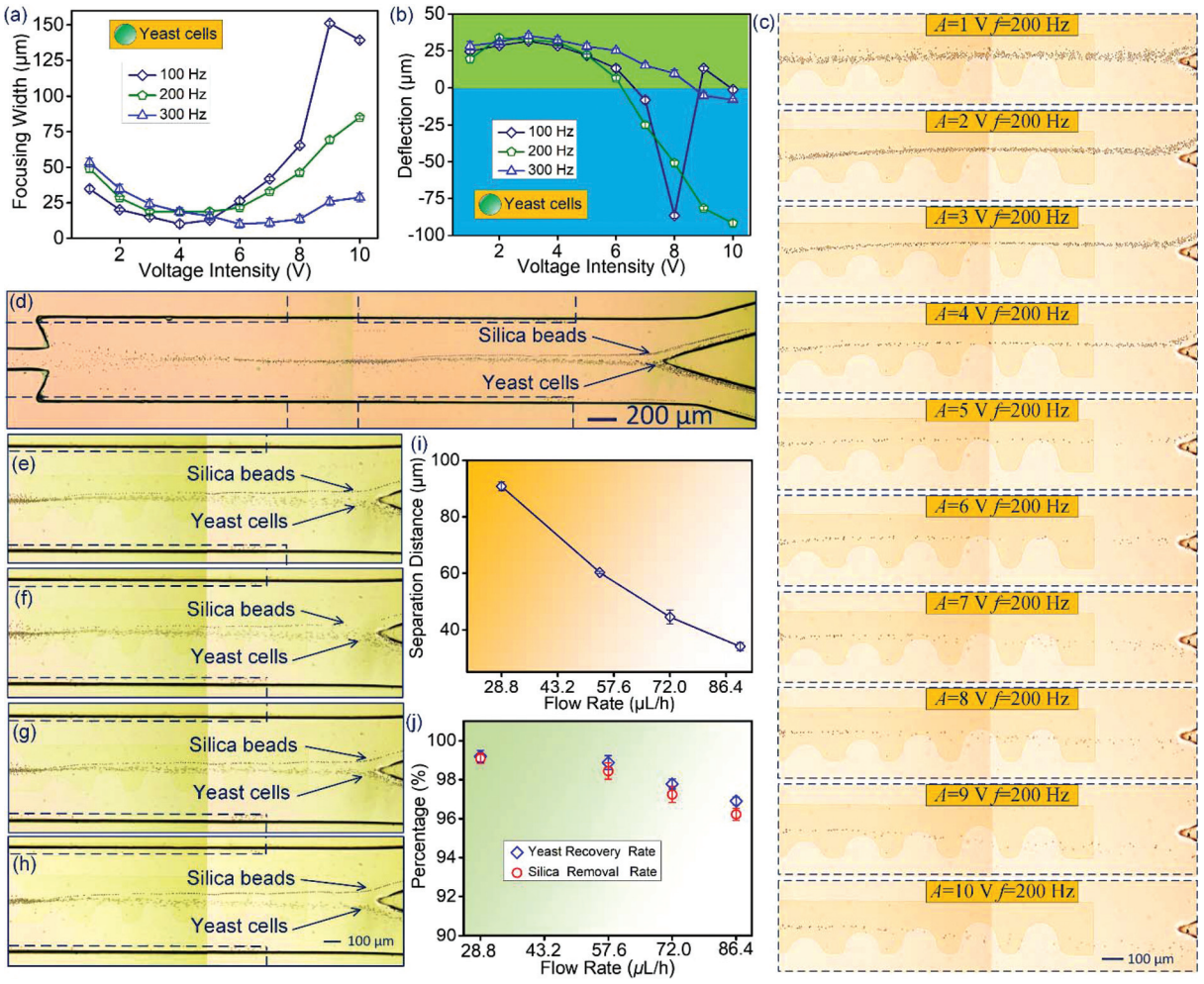

Fig. 8 Separation process of yeast cells and silica particles at f_1 = 100 Hz, A_1 = 3 V, f_2 = 100 Hz and A_2 = 7 V. (a) and (b) Focusing and deflection characterization of yeast cells on the designed floating electrode. (c) Image sequence illustrating the particle behaviors under different voltage intensities. (d) Micrograph of the overall separation process. (e–h) Separation under different flow rates: (b) 86.4 μL h^{-1}, (c) 72 μL h^{-1}, (d) 57.6 μL h^{-1}, (e) 28.8 μL h^{-1}. (i) Dependence of separation distance on flow rate. (j) Dependence of separation efficiency on flow rate.

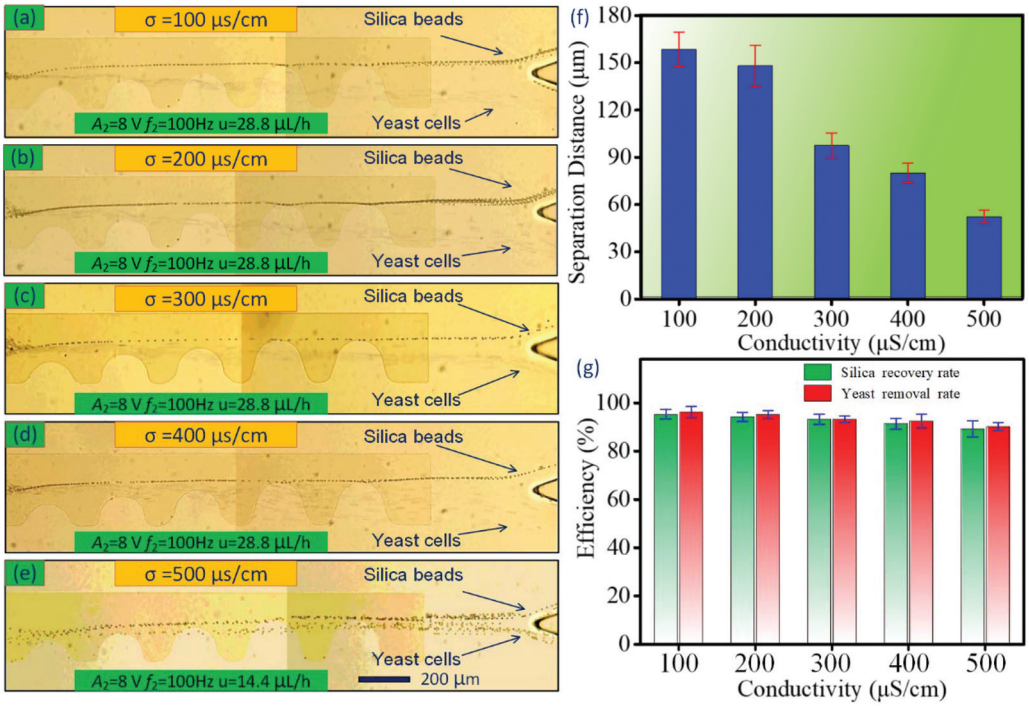

Fig. 9 Conductivity dependence of the separation process at A_2 = 8 V and f_2 = 100 Hz. (a–e) Separation process at various conductivities: (a) 100 μS cm^{-1}, (b) 200 μS cm^{-1}, (c) 300 μS cm^{-1}, (d) 400 μS cm^{-1}, (e) 500 μS cm^{-1}. (f/g) Effect of conductivity on the separation distance/efficiency.

(Fig. 9d). When the conductivity was 500 μS cm^{-1}, we also obtained the acceptable separation result by properly reducing the flow rate to 14.4 μL h^{-1}, obtaining the separation efficiency of 90.1% and the separation distance of 42.23 μm (Fig. 9e). Histograms demonstrating separation distance and efficiency against conductivity are summarized in Fig. 9f and g, respectively.

Conclusions

We proposed a novel method of particle separation involving two modules, the upstream ICEO-based particle module for focusing and the downstream AICEO-based module for separation. From a theoretical study of the AICEO vortex profile and the flow-field distributions on the arc-edge-based floating electrode, we first demonstrated the separation principle and analyzed the detail mechanisms in the density- and size-based separation. Then, we classified the AICEO characterization of particles experimentally and found a common characteristic of the particle AICEO characterization that the particle stream underwent a left deflection ending up in outlet A under the dominating buoyancy force but experienced a right deflection ending up in outlet B with the levitation force dominating. Next, depending on the numerical study of the sensitivity of this method in density-based separation, we separated 4 μm PMMA and 4 μm silica particles to verify the capability of our separation approach in density-based separation at f_1 = 100 Hz, A_1 = 3 V, f_2 = 200 Hz, A_2 = 10 V and u = 43.2 μL h^{-1}, obtaining nearly 100% focusing efficiency in the focusing region and 98% separation efficiency in the separation region. Besides, we also explored the effect of inlet velocity on the separation capability and found that the separation efficiency always exceeded 96% at u = 28.8–72 μL h^{-1}. Subsequently, we studied numerically the sensitivity of this method in size-based separation, and experimentally validated its feasibility by separating multi-sized yeast cells, obtaining good separation results. Finally, we extracted yeast cells using this method, obtaining a purity exceeding 98% at f_1 = 100 Hz, A_1 = 3 V, f_2 = 100 Hz, A_2 = 7 V and u = 28.8 μL h^{-1}. Moreover, we also studied the conductivity-dependent separation performance and found that this method can realize high-efficiency separation at the conductivity from 10 to 500 μS cm^{-1}. The main advantages of this method, gentle separation environment, contact-free separation process, high-sensitivity and high-efficiency separation capability, make it a potential alternative in environmental monitoring, transesterification of microalgal lipids to biodiesel, and solar cell technology.

Conflicts of interest

There are no conflicts to declare.

Acknowledgements

This study was funded by the National Natural Science Foundation of China (No. 11672095, 11872165, and 11802078),

the Self-Planned Task (SKLRS201803B) of State Key Laboratory of Robotics and System (HIT), and the Opening fund of State Key Laboratory of Nonlinear Mechanics.

Notes and references

1 J. C. Chow, J. G. Watson, M. C. Green, X. Wang, L. A. Chen, D. L. Trimble, P. M. Cropper, S. D. Kohl and S. B. Gronstal, *J. Air Waste Manage. Assoc.*, 2018, **68**, 494–510.
2 G. F. Pauli, S. M. Pro, L. R. Chadwick, T. Burdick, L. Pro, W. Friedl, N. Novak, J. Maltby, F. Qiu and J. B. Friesen, *Anal. Chem.*, 2015, **87**, 7418–7425.
3 X. Lu, C. Liu, G. Hu and X. Xuan, *J. Colloid Interface Sci.*, 2017, **500**, 182–201.
4 C. Liu, B. Ding, C. Xue, Y. Tian, G. Hu and J. Sun, *Anal. Chem.*, 2016, **88**, 12547–12553.
5 M. Wu, Z. Mao, K. Chen, H. Bachman, Y. Chen, J. Rufo, L. Ren, P. Li, L. Wang and T. J. Huang, *Adv. Funct. Mater.*, 2017, **27**, 1606039.
6 S. H. Holm, J. P. Beech, M. P. Barrett and J. O. Tegenfeldt, *Anal. Methods*, 2016, **8**, 3291–3300.
7 A. Dalili, E. Samiei and M. Hoorfar, *Analyst*, 2018, **144**, 87–113.
8 J. Wu, Q. Chen and J. M. Lin, *Analyst*, 2017, **142**, 421–441.
9 P. Arosio, T. Muller, L. Mahadevan and T. P. Knowles, *Nano Lett.*, 2014, **14**, 2365–2371.
10 D. Li, X. Lu and X. Xuan, *Anal. Chem.*, 2016, **88**, 12303–12309.
11 D. Das, D. T. Phan, Y. Zhao, Y. Kang, V. Chan and C. Yang, *Electrophoresis*, 2017, **38**, 645–652.
12 E. J. Fong, A. C. Johnston, T. Notton, S. Y. Jung, K. A. Rose, L. S. Weinberger and M. Shusteff, *Analyst*, 2014, **139**, 1192–1200.
13 M. Wu, Y. Ouyang, Z. Wang, R. Zhang, P. H. Huang, C. Chen, H. Li, P. Li, D. Quinn, M. Dao, S. Suresh, Y. Sadovsky and T. J. Huang, *Proc. Natl. Acad. Sci. U. S. A.*, 2017, **114**, 10584–10589.
14 J. Xuan and M. L. Lee, *Anal. Methods*, 2014, **6**, 27–37.
15 J. K. Lim, D. C. Chieh, S. A. Jalak, P. Y. Toh, N. H. Yasin, B. W. Ng and A. L. Ahmad, *Small*, 2012, **8**, 1683–1692.
16 U. Tallarek, F. C. Leinweber and I. Nischang, *Electrophoresis*, 2005, **26**, 391–404.
17 C. Cui, J. Huang, J. Huang and G. Chen, *Electrochim. Acta*, 2017, **258**, 793–799.
18 S. Yoo and B. Kang, *Electrochim. Acta*, 2015, **151**, 270–275.
19 W. Al-Faqheri, T. H. G. Thio, M. A. Qasaimeh, A. Dietzel, M. Madou and A. A. Al-Halhouli, *Microfluid. Nanofluid.*, 2017, **21**, 102.
20 C. Liu, C. Xue, X. Chen, L. Shan, Y. Tian and G. Hu, *Anal. Chem.*, 2015, **87**, 6041–6048.
21 F. Tian, W. Zhang, L. Cai, S. Li, G. Hu, Y. Cong, C. Liu, T. Li and J. Sun, *Lab Chip*, 2017, **17**, 3078–3085.
22 Q. Chen, D. Li, J. Lin, M. Wang and X. Xuan, *Anal. Chem.*, 2017, **89**, 6915–6920.
23 R. Zhou, Q. Yang, F. Bai, J. A. Werner, H. Shi, Y. Ma and C. Wang, *Microfluid. Nanofluid.*, 2016, **20**, 110.
24 X. Hu, P. H. Bessette, J. Qian, C. D. Meinhart, P. S. Daugherty and H. T. Soh, *Proc. Natl. Acad. Sci. U. S. A.*, 2005, **102**, 15757–15761.
25 N. Lewpiriyawong, K. Kandaswamy, C. Yang, V. Ivanov and R. Stocker, *Anal. Chem.*, 2011, **83**, 9579–9585.
26 K. Zhao, R. Peng and D. Li, *Nanoscale*, 2016, **8**, 18945–18955.
27 M. Li, S. Li, W. Cao, W. Li, W. Wen and G. Alici, *Microfluid. Nanofluid.*, 2012, **14**, 527–539.
28 S.-H. Liao, I. F. Cheng and H.-C. Chang, *Microfluid. Nanofluid.*, 2011, **12**, 201–211.
29 S. H. Ling, Y. C. Lam and C. H. Kua, *Microfluid. Nanofluid.*, 2011, **11**, 579–591.
30 J. Gao, R. Riahi, M. L. Sin, S. Zhang and P. K. Wong, *Analyst*, 2012, **137**, 5215–5221.
31 I. J. Benczik, Z. Toroczkai and T. Tel, *Phys. Rev. Lett.*, 2002, **89**, 164501.
32 R. D. Vilela and A. E. Motter, *Phys. Rev. Lett.*, 2007, **99**, 264101.
33 E. Balkovsky, G. Falkovich and A. Fouxon, *Phys. Rev. Lett.*, 2001, **86**, 2790–2793.
34 J.-R. Angilella, R. D. Vilela and A. E. Motter, *J. Fluid Mech.*, 2014, **744**, 183–216.
35 I. Lazo, C. Peng, J. Xiang, S. V. Shiyanovskii and O. D. Lavrentovich, *Nat. Commun.*, 2014, **5**, 5033.
36 A. J. Pascall and T. M. Squires, *Phys. Rev. Lett.*, 2010, **104**, 088301.
37 R. Peng and D. Li, *Nanoscale*, 2016, **8**, 12237–12246.
38 T. M. Squires and M. Z. Bazant, *J. Fluid Mech.*, 2004, **509**, 217–252.
39 X. Xuan and D. Li, *J. Colloid Interface Sci.*, 2005, **289**, 291–303.
40 Y. Ren, W. Liu, Y. Jia, Y. Tao, J. Shao, Y. Ding and H. Jiang, *Lab Chip*, 2015, **15**, 2181–2191.
41 Y. Ren, W. Liu, J. Liu, Y. Tao, Y. Guo and H. Jiang, *Biomicrofluidics*, 2016, **10**, 054103.
42 Y. Ren, W. Liu, Z. Wang and Y. Tao, *Phys. Fluids*, 2018, **30**, 062006.
43 W. Liu, J. Shao, Y. Ren, J. Liu, Y. Tao, H. Jiang and Y. Ding, *Biomicrofluidics*, 2016, **10**, 034105.
44 Y. Ren, J. Liu, W. Liu, Q. Lang, Y. Tao, Q. Hu, L. Hou and H. Jiang, *Lab Chip*, 2016, **16**, 2803–2812.
45 X. Chen, Y. Ren, W. Liu, X. Feng, Y. Jia, Y. Tao and H. Jiang, *Anal. Chem.*, 2017, **89**, 9583–9592.
46 Y. Jia, Y. Ren and H. Jiang, *RSC Adv.*, 2015, **5**, 66602–66610.
47 X. Chen, Y. Ren, L. Hou, X. Feng, T. Jiang and H. Jiang, *Nanoscale*, 2019, **11**, 6410–6421.
48 Y. Ren, C. Song, W. Liu, T. Jiang, J. Song, Q. Wu and H. Jiang, *Electrophoresis*, 2019, **40**, 979–992.
49 H. Sun, Y. Ren, W. Liu, X. Feng, L. Hou, Y. Tao and H. Jiang, *Anal. Chem.*, 2018, **90**, 11376–11384.
50 J. Chen, Y. Li, L. Huang, N. Jia, C. Li and G. Shi, *Adv. Mater.*, 2015, **27**, 3654–3660.

51 X. Sun, D. Luo, J. Liu and D. G. Evans, *ACS Nano*, 2010, **4**, 3381–3389.
52 K. Zhang, Y. Ren, Y. Tao, W. Liu, T. Jiang and H. Jiang, *Anal. Chem.*, 2019, **91**, 4457–4465.
53 V. Lecault, M. Vaninsberghe, S. Sekulovic, D. J. Knapp, S. Wohrer, W. Bowden, F. Viel, T. McLaughlin, A. Jarandehei, M. Miller, D. Falconnet, A. K. White, D. G. Kent, M. R. Copley, F. Taghipour, C. J. Eaves, R. K. Humphries, J. M. Piret and C. L. Hansen, *Nat. Methods*, 2011, **8**, 581–586.
54 S. Son, A. Tzur, Y. Weng, P. Jorgensen, J. Kim, M. W. Kirschner and S. R. Manalis, *Nat. Methods*, 2012, **9**, 910–912.
55 M. R. Bennett, W. L. Pang, N. A. Ostroff, B. L. Baumgartner, S. Nayak, L. S. Tsimring and J. Hasty, *Nature*, 2008, **454**, 1119–1122.
56 M. Z. Bazant and T. M. Squires, *Phys. Rev. Lett.*, 2004, **92**, 066101.
57 K. H. Kang, Y. Kang, X. Xuan and D. Li, *Electrophoresis*, 2006, **27**, 694–702.